



ELSEVIER

Available online at [www.sciencedirect.com](http://www.sciencedirect.com)

SCIENCE @ DIRECT®

Continental Shelf Research 25 (2005) 373–396

CONTINENTAL SHELF  
RESEARCH

[www.elsevier.com/locate/csr](http://www.elsevier.com/locate/csr)

# Observations of plan-view sand ripple behavior and spectral wave climate on the inner shelf of San Pedro Bay, California

J.P. Xu

*US Geological Survey, MS 999, 345 Middlefield Rd., Menlo Park, CA 94025, USA*

Received 11 December 2003; received in revised form 4 August 2004; accepted 1 October 2004  
Available online 30 November 2004

## Abstract

Concurrent video images of sand ripples and current meter measurements of directional wave spectra are analyzed to study the relations between waves and wave-generated sand ripples. The data were collected on the inner shelf off Huntington Beach, California, at 15 m water depth, where the sea floor is comprised of well-sorted very fine sands ( $D_{50} = 92 \mu\text{m}$ ), during the winter of 2002. The wave climate, which was controlled by southerly swells (12–18 s period) and westerly wind waves (5–10 s period), included three wave types: (A) uni-modal, swells only; (B) bi-modal, swells dominant; and (C) bi-modal, wind-wave dominant. Each wave type has distinct relations with the plan-view shapes of ripples that are classified into five types: (1) sharp-crested, two-dimensional (2-D) ripples; (2) sharp-crested, brick-pattern, 3-D ripples; (3) bifurcated, 3-D ripples; (4) round-crested, shallow, 3-D ripples; and (5) flat bed. The ripple spacing is very small and varies between 4.5 and 7.5 cm. These ripples are anorbital as ripples in many field studies. Ripple orientation is only correlated with wave directions during strong storms (wave type C). In a poly-modal, multi-directional spectral wave environment, the use of the peak parameters (frequency, direction), a common practice when spectral wave measurements are unavailable, may lead to significant errors in boundary layer and sediment transport calculations.

© 2004 Elsevier Ltd. All rights reserved.

*Keywords:* Anorbital ripples; Directional wave spectra; Fine sand

## 1. Introduction

Bed roughness is one of the controlling factors in bottom boundary layer dynamics and sediment transport. Wave-generated sand ripples are probably the most common bedforms on continental

shelves to directly affect the roughness calculations. Since the pioneering work of Inman (1957), numerous studies on wave-generated sand ripples have been conducted both in laboratories (Yalin and Russell, 1962; Inman and Bowen, 1963; Carstens et al., 1969; Mogridge and Kamphuis, 1972; Lofquist, 1978; Willis et al., 1993) and in the field (Dingler, 1974; Karl et al., 1980; Miller and

*E-mail address:* [jpx@usgs.gov](mailto:jpx@usgs.gov) (J.P. Xu).

Komar, 1980; Boyd et al., 1988; Amos et al., 1988; Osborne and Vincent, 1993; Jette and Hanes, 1996; Traykovski et al., 1999). Clifton (1976) analyzed data from some of the mentioned studies and summarized sand ripples into three basic categories: orbital (mainly from laboratory data), anorbital (mainly from field data), and suborbital (a transition stage between the first two). This characterization has since been updated and strengthened thanks to the analytical works of Nielsen (1981), Grant and Madsen (1982), and Wiberg and Harris (1994) and the availability of more detailed bedform measurements of Hay and Wilson (1994), Traykovski et al. (1999), and Faraci and Foti (2002). Most of the data from previous studies, especially the field measurements, present more detailed descriptions of physical and geometrical properties of ripples than of the properties of waves, currents, and other hydrodynamic variables. One important aspect that has not been fully investigated is how sand ripples respond to two coexisting wave trains of different frequencies and approaching from two different directions. Karl et al. (1980) and Miller and

Komar (1980) speculated on the superimposition of two such wave trains and their impact on forming sand ripples, but lack of simultaneous wave and ripple data made those efforts inconclusive.

The purpose of this paper is to present and analyze 20 days of data collected on the inner shelf of San Pedro Bay, California. This data set includes simultaneous time series of directional wave spectra and video footage of sand ripples. It will allow us (1) to categorize the types of surface waves as well as the types of bedforms, (2) to examine the variability and intrinsic relations between ripples (patterns, spacing, etc.) and the wave types, and (3) to investigate how bedforms respond to the variability of poly-modal, multi-directional wave conditions.

## 2. Setting

The data were obtained from instruments on a tripod that was deployed in 15 m of water off Huntington Beach, California (Fig. 1). It was one

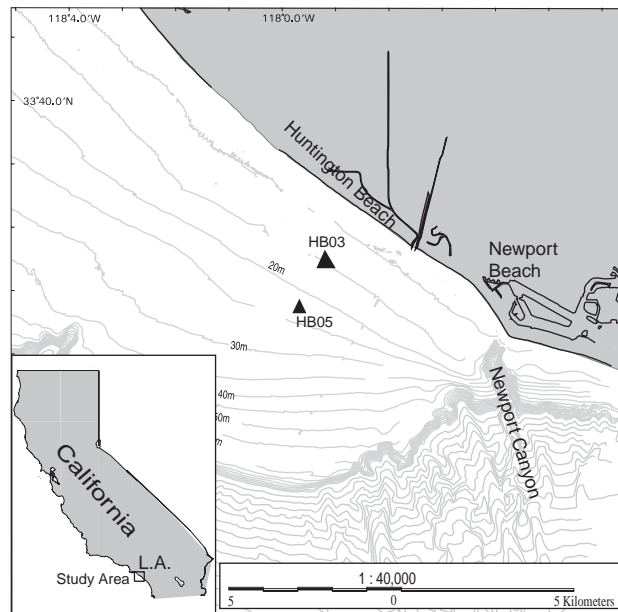


Fig. 1. Bathymetry and location of the study site. The instruments were on a tripod deployed in 15 m water depth at the HB03 site. The video camera was 47 cm above the sea floor. The upward-looking ADCP was 1.2 m above the sea floor.

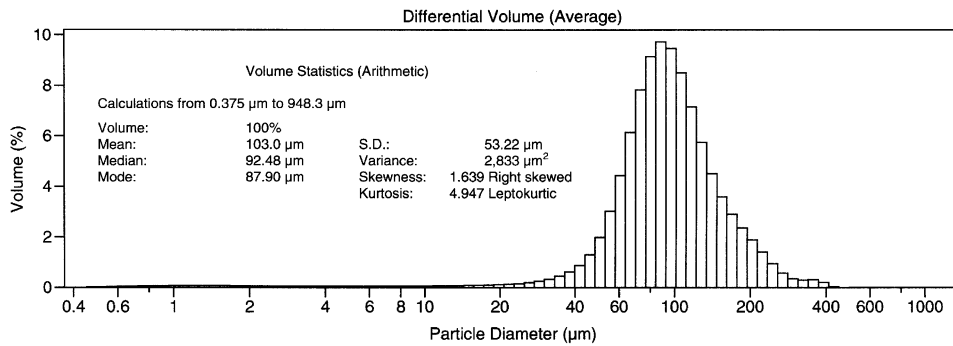


Fig. 2. Grain size distribution from a laser particle size analyzer showing well-sorted fine sands at the HB03 site. Moment statistics are also shown.

of three instrumented platforms that were deployed on the eastern San Pedro shelf by the US Geological Survey's Huntington Beach Investigation project (Noble et al., 2003). The study site (HB03, 33°37.598'N, 117°59.227'W) is on the upper shoreface of a smooth, moderately wide, but very shallow continental shelf. The shelf is 8.5 km wide, and the water depth at the shelf break is only 60 m. The shelf is covered with a thin (3–20 m) veneer of undifferentiated late Quaternary sediment punctured in places by outcrops of Tertiary rocks (Karl et al., 1980). The study site is on a patch of well-sorted, fine to very fine sand with a median diameter ( $D_{50}$ ) of 92 μm and standard deviation of 53 μm (Fig. 2). The cohesiveness of the ~5% of grains (<64 μm) is unknown thus its effect on sand ripples is assumed negligible. Tidal currents on the shelf, mainly semi-diurnal, are relatively weak as compared to the subtidal flows. Subtidal currents on the shelf are typically 5–10 cm/s; tidal currents rarely exceed 10 cm/s (Drake et al., 1985; Noble et al., 2003). Sea-breeze in the study area can generate a relatively strong periodic current fluctuation of 24 h, but it is mostly limited to depths above the thermocline (Hamilton et al., 2001; Noble et al., 2003). Surface waves approach the San Pedro shelf along corridors from the west and south (Karl et al., 1980). Islands and banks tend to damp out long-period (15–20 s) swells from the west and leave short-period (7–10 s) waves to continue relatively free of interference, but swells from the Southern Hemisphere reach the shelf without

interruption (Horrer, 1950). Long-term observations by NOAA from a drilling platform in southern San Pedro Bay indicate that significant wave height ( $H_s$ ) is typically 0.5–0.7 m in April–October and increases to about 1 m with occasional storm peaks to 2.5 m during November–March (Drake et al., 1985). Internal waves with periods ranging from 24 min to 6 h have been observed in northern San Pedro Bay (Karl et al., 1980), but empirical calculation (from Cacchione and Southard, 1974) by Karl et al. (1980) concluded that internal waves alone are not significant in initiating sediment movement.

### 3. Methods and data

Two field experiments (each four months long) were conducted during the summer/fall of 2001 and the winter of 2002. Each experiment had moorings and/or instrumented tripods occupying 13 sites between 15 and 60 m water depth on the shelf off Huntington Beach, California (Noble et al., 2003). Only the data from one tripod (HB03 in 15 m of water, see Fig. 1) during the winter deployment (January 16–April 15, 2002) are discussed here. This tripod was equipped with a suite of instruments that collect oceanographic and sediment data near the bed as well as through the water column, but the focus of this paper is on: (1) video footage from a digital camera system; and (2) directional wave spectra from an acoustic

Doppler current profiler (ADCP) (RD Instruments, 2001).

A video camera (SONY digital 8 Handycam) was mounted on the tripod to take video footage of the sea floor. The glass window of the optics at the bottom of the water-tight housing was 47 cm above the bed. The video camera was customized with a controller board that determined the timing and length of the taping: it turned on the camera and a synchronized strobe for 90 s every 6 h. The digital tape (capacity of 90 min) ran out on February 7, 2002 when bio-fouling had just begun to block the view through the glass window. Except for a period of several hours when a strong storm passed the area, clear images of the sea bed were recorded. Over a period of 20 days (January 17–February 7, 2002) the bedforms on the sea floor changed with hydrodynamic conditions: from sheet-flow to different sizes and shapes of sand ripples to a smooth, featureless bed. There was no time-series measurement of the distance between the camera and sea bed. Judging from the video images, it appears that the scour/settling around the footpad of the tripod was negligible. Within each 90-s segment, the change of ripple properties (shapes, ripple spacing) was negligible although one can see the oscillatory movement of sand grains over the ripples. A still frame was captured from each 90-s segment to represent the sand ripple status in that segment of footage. There are 82 still frames in total (Fig. 3).

There is no scaling reference in the field video footage; therefore, a reference image with a linear scale had to be created in order to measure the ripple spacing. A flattened wire mesh with a 1-in (2.54 cm) grid was placed on the bottom of a water tank. The camera system with the same lens and optics was assembled and submerged in water with the glass window of the camera housing positioned the same distance between the sea bed and the camera on the tripod during deployment. Several identical reference images were taken, one of which is plotted in Fig. 3. Ripple spacings (distance between crests) are manually measured by scaling the field video footage against the reference frame. A trace of the reference grid was overlaid on each frame to aid the measurement. In order to avoid errors due to optical distortion on

the edges of the images, which can be clearly seen in both the reference image and the field video footage, only the ripples in the smaller rectangle were measured. This measuring area ( $43 \times 33 \text{ cm}^2$ ) was also intentionally placed away from the footpad to discount the possible contamination from the footpad. The number of available ripples in the rectangular area varied significantly (between 3 and 10). The statistics of these measurements (mean and 95% confidence interval) are presented in Table 1.

Because there was no compass information available to the camera system, the ripple orientations had to be obtained in a rather cumbersome way. First it was assumed that under a uni-modal, high energy wave spectrum the ripple orientation is perpendicular to the direction of wave propagation, as is the case of monochromatic waves. One such spectrum was identified, and then principal component analysis was applied to the two horizontal velocity components (East (u) and North (v)) measured from the first bin of the ADCP to estimate the azimuth and eccentricity. This azimuth was plotted on to the corresponding image of ripples. The ripple orientation in this and all other images was measured relative to this azimuth. For the brick-pattern (type 2) ripples, the orientations were measured from the more dominant set of ripples (the bridges in Sleath, 1984). This set of ripples was also roughly parallel to, or in a small angle with, the type 1 ripples. For type 3 ripples, the oblique branches had to be ignored in order to determine the 'dominant' orientation in the whole square measuring area. Foreign objects on the sea floor seem to have substantial effect on ripple orientations. In addition to the footpad of the tripod, hermit crabs tended to aggregate at times near the footpad and under the spot light near the center of the image. Thus, ripple orientations were not available from several images.

The ADCP was placed on top of the tripod, 1.23 m above the sea bed. It recorded mean current velocity (an average of a 45-s ensemble) every 3 min in 12 vertical bins, at a spatial interval of 1 m, through the water column. In addition, it also recorded 17 min, at a sampling frequency of 2 Hz, of pressure, beam velocities, and surface tracking

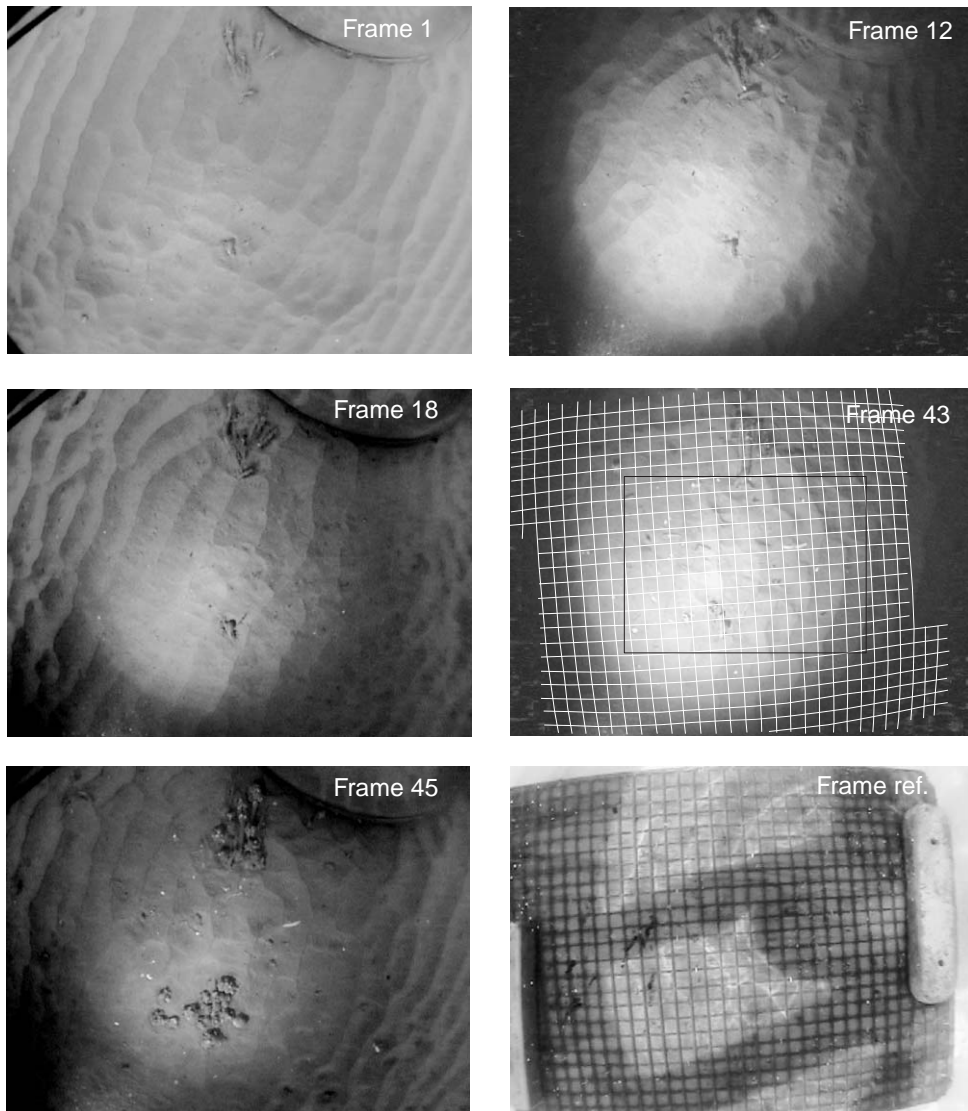


Fig. 3. Still frames captured from the video tape showing ripples at different times of the deployment. Part of the footpad of the tripod and a section of cables can be seen on the top right and left corners of the images. See Table 1 for wave and ripple measurements corresponding to each frame number. The wire mesh (1 in = 2.54 cm grid) provides a scale for ripple spacing measurement. Ripple measurements are taken from the smaller rectangle ( $43 \times 33 \text{ cm}^2$ ) to avoid optical distortion.

every hour for directional wave spectra calculations (Terray et al., 1999; Rorbaek and Andersen, 2000; Strong et al., 2000). Wave spectra were computed using RDI's WaveMon and WaveView software (RD Instruments, 2001). The frequency spectrum and directional spreading were first calculated over an FFT length of 1024 data points,

then binned into 128 frequency and 90 directional bands to form the directional wave spectra (Fig. 4). The frequency spectra calculated from either the pressure or the beam velocity data are almost identical. The pressure spectra are used in the calculations described in the subsequent sections.

Table 1  
A summary of wave and ripple measurements

Frame no./ date	Wave types	$H_s$ (m)	$T_{p,ses}$ (s)	$T_{p,bovs}$ (s)	Peak wave direction	HB03 azimuth	HB05 azimuth	$U_{rms}$ (m/s)	$d_0$ (m)	Ripple types	Ripple orientation (deg.)	Ripple spacing $\lambda$ (cm)
1	A	1.3	15.7	15.7	160	230	186	0.19	0.98	1	255	7.0±0.5
2 (1/18)	A	1.4	15.7	15.7	175	234	176	0.19	0.98	1	254	6.9±0.4
3	A	1.2	15.7	15.7	171	218	209	0.20	0.99	2	254	7.3±0.4
4	A	1.2	15.1	15.1	166	214	179	0.18	0.88	2	254	7.0±0.2
5	B	1.8	15.1	15.1	169	233	186	0.27	1.31	2	253	7.0±0.4
6 (1/19)	B	1.6	15.4	15.4	188	229	193	0.26	1.27	2	251	7.0±0.4
7	B	1.5	12.3	14.8	179	259	216	0.21	0.98	2	253	7.5±0.5
8	B	1.2	14.3	14.3	179	252	203	0.17	0.79	2	253	7.2±0.6
9	B	1.2	11.7	11.7	171	244	212	0.17	0.65	3	254	6.8±0.4
10 (1/20)	B	1.2	13.5	13.5	171	208	206	0.18	0.77	3	255	6.3±0.4
11	B	1.1	11.4	13.5	180	233	212	0.16	0.68	3	255	7.3±0.7
<b>12</b>	<b>C</b>	<b>1.7</b>	<b>9.2</b>	<b>14.0</b>	<b>237</b>	<b>266</b>	<b>260</b>	<b>0.23</b>	<b>1.02</b>	<b>3</b>	<b>253</b>	<b>5.9±0.3</b>
<b>13</b>	<b>C</b>	<b>1.3</b>	<b>12.5</b>	<b>12.5</b>	<b>171</b>	<b>259</b>	<b>231</b>	<b>0.18</b>	<b>0.74</b>	<b>3</b>	<b>251</b>	<b>6.1±0.3</b>
14 (1/21)	C	1.2	8.8	8.8	222	255	223	0.18	0.50	3	252	6.1±0.2
15	C	1.4	10.0	10.0	233	251	237	0.21	0.66	3	251	6.3±0.3
16	B	1.2	11.7	13.2	179	247	218	0.18	0.77	3	254	5.7±0.2
17	B	1.2	11.0	16.7	171	238	209	0.18	0.95	3	254	6.3±0.3
18 (1/22)	B	1.2	16.1	18.3	179	246	216	0.20	1.17	3	253	6.8±0.6
19	B	1.6	17.1	17.1	212	251	244	0.25	1.36	2	251	6.5±0.3
<b>20</b>	<b>C</b>	<b>1.9</b>	<b>8.0</b>	<b>10.9</b>	<b>243</b>	<b>258</b>	<b>214</b>	<b>0.26</b>	<b>0.91</b>	<b>1</b>	<b>257</b>	<b>5.9±0.3</b>
<b>21</b>	<b>C</b>	<b>2.1</b>	<b>6.8</b>	<b>16.0</b>	<b>243</b>	<b>265</b>	<b>251</b>	<b>0.27</b>	<b>1.39</b>	<b>1</b>	<b>260</b>	<b>5.9±0.5</b>
<b>22 (1/23)</b>	<b>C</b>	<b>2.2</b>	<b>12.9</b>	<b>15.7</b>	<b>239</b>	<b>248</b>	<b>249</b>	<b>0.31</b>	<b>1.54</b>	<b>1</b>	<b>260</b>	<b>5.2±0.6</b>
<b>23</b>	<b>C</b>	<b>2.6</b>	<b>8.6</b>	<b>8.6</b>	<b>239</b>	<b>263</b>	<b>253</b>	<b>0.34</b>	<b>0.93</b>	<b>5</b>		
<b>24</b>	<b>C</b>	<b>2.1</b>	<b>10.4</b>	<b>13.3</b>	<b>240</b>	<b>258</b>	<b>249</b>	<b>0.28</b>	<b>1.18</b>	<b>3</b>		<b>5.7±0.2</b>
<b>25</b>	<b>C</b>	<b>1.8</b>	<b>15.1</b>	<b>15.1</b>	<b>182</b>	<b>257</b>	<b>227</b>	<b>0.26</b>	<b>1.24</b>	<b>3</b>	<b>261</b>	<b>5.6±0.3</b>
<b>26 (1/24)</b>	<b>B</b>	<b>1.7</b>	<b>10.6</b>	<b>12.7</b>	<b>175</b>	<b>248</b>	<b>232</b>	<b>0.25</b>	<b>1.02</b>	<b>2</b>	<b>254</b>	<b>5.3±0.2</b>
27	B	1.4	14.0	14.0	207	242	232	0.21	0.95	3	252	5.2±0.2
28	B	1.1	13.7	13.7	183	250	230	0.17	0.72	3	247	5.3±0.6
29	B	1.1	13.7	13.7	171	223	231	0.16	0.69	1	249	5.1±0.3
30 (1/25)	B	1.0	13.0	13.0	232	237	218	0.16	0.65	3	247	4.7±0.3
31	A	0.7	13.2	13.2	237	241	223	0.11	0.47	4	252	5.5±0.5
32	A	1.0	14.0	14.0	231	245	201	0.14	0.63	4	252	5.4±0.2
33	A	0.8	11.6	12.0	171	238	217	0.13	0.50	4	252	5.0±0.2
34 (1/26)	A	0.8	11.7	13.8	171	224	210	0.12	0.53	4	252	5.2±0.3
35	A	0.7	13.7	13.7	171	222	193	0.11	0.50	4		
36	B	0.9	15.3	15.3	175	226	190	0.14	0.69	5		
37	B	1.0	10.0	13.3	173	244	189	0.14	0.58	5		
38 (1/27)	B	1.1	10.8	13.5	249	223	193	0.14	0.60	5		
39	B	1.0	10.8	15.1	175	239	190	0.13	0.62	5		
40	B	0.9	13.5	14.7	171	230	196	0.15	0.70	5		
41	B	0.9	13.9	15.3	215	223	188	0.13	0.64	5		
42 (1/28)	B	1.3	13.5	13.5	215	232	221	0.23	0.98	4	246	5.1±0.5
<b>43</b>	<b>C</b>	<b>1.6</b>	<b>11.2</b>	<b>13.8</b>	<b>171</b>	<b>233</b>	<b>221</b>	<b>0.25</b>	<b>1.11</b>	<b>1</b>	<b>244</b>	<b>4.6±0.3</b>
<b>44</b>	<b>C</b>	<b>1.7</b>	<b>4.8</b>	<b>14.4</b>	<b>258</b>	<b>248</b>	<b>227</b>	<b>0.19</b>	<b>0.90</b>	<b>1</b>	<b>240</b>	<b>5.7±0.3</b>
45	C	1.6	7.6	12.2	249	252	233	0.20	0.77	3	239	5.5±0.3
46 (1/29)	B	1.5	11.9	11.9	219	247	231	0.21	0.81	1	239	5.3±0.2
47	B	1.2	13.5	15.9	219	255	237	0.18	0.90	3	242	5.7±0.2
48	B	1.5	15.2	15.2	215	250	222	0.20	0.98	3	242	5.6±0.3
49	B	1.3	12.1	13.8	183	238	228	0.18	0.79	1	250	5.3±0.2
50 (1/30)	B	1.3	9.9	9.9	228	253	230	0.18	0.57	1	245	5.4±0.2

Table 1. (continued)

Frame no./ date	Wave types	$H_s$ (m)	$T_{p,ses}$ (s)	$T_{p,bovs}$ (s)	Peak wave direction	HB03 azimuth	HB05 azimuth	$U_{rms}$ (m/s)	$d_0$ (m)	Ripple types	Ripple orientation (deg.)	Ripple spacing $\lambda$ (cm)
<b>51</b>	<b>B</b>	<b>1.3</b>	<b>8.1</b>	<b>10.1</b>	<b>227</b>	<b>256</b>	<b>239</b>	<b>0.17</b>	<b>0.54</b>	<b>1</b>	<b>253</b>	<b>5.8±0.5</b>
<b>52</b>	<b>C</b>	<b>1.5</b>	<b>8.6</b>	<b>9.1</b>	<b>224</b>	<b>259</b>	<b>248</b>	<b>0.19</b>	<b>0.53</b>	<b>1</b>	<b>255</b>	<b>5.4±0.4</b>
<b>53</b>	<b>C</b>	<b>1.5</b>	<b>9.1</b>	<b>9.1</b>	<b>234</b>	<b>266</b>	<b>261</b>	<b>0.19</b>	<b>0.54</b>	<b>1</b>	<b>254</b>	<b>6.1±0.6</b>
<b>54 (1/31)</b>	<b>C</b>	<b>1.5</b>	<b>8.5</b>	<b>9.1</b>	<b>232</b>	<b>260</b>	<b>252</b>	<b>0.19</b>	<b>0.56</b>	<b>1</b>	<b>254</b>	<b>6.8±0.5</b>
<b>55</b>	<b>C</b>	<b>2.2</b>	<b>6.2</b>	<b>8.9</b>	<b>252</b>	<b>267</b>	<b>256</b>	<b>0.22</b>	<b>0.63</b>	<b>1</b>	<b>255</b>	<b>6.1±0.2</b>
<b>56</b>	<b>C</b>	<b>1.6</b>	<b>6.3</b>	<b>10.6</b>	<b>231</b>	<b>263</b>	<b>250</b>	<b>0.19</b>	<b>0.62</b>	<b>1</b>	<b>255</b>	<b>6.3±0.3</b>
<b>57</b>	<b>C</b>	<b>1.2</b>	<b>8.9</b>	<b>8.9</b>	<b>243</b>	<b>268</b>	<b>248</b>	<b>0.14</b>	<b>0.41</b>	<b>3</b>	<b>256</b>	<b>6.0±0.3</b>
<b>58 (2/1)</b>	<b>C</b>	<b>1.0</b>	<b>8.4</b>	<b>11.7</b>	<b>232</b>	<b>261</b>	<b>243</b>	<b>0.12</b>	<b>0.47</b>	<b>3</b>	<b>253</b>	<b>6.0±0.3</b>
59	C	0.8	8.0	8.5	236	259	254	0.09	0.25	4		
60	B	0.6	10.2	10.9	235	253	241	0.08	0.27	5		
61	B	0.6	10.9	10.9	171	248	233	0.09	0.30	5		
62 (2/2)	B	0.6	7.3	14.2	179	246	201	0.08	0.34	5		
63	A	0.8	15.4	15.4	215	241	230	0.12	0.59	5		
64	A	0.9	15.1	15.1	211	237	225	0.15	0.72	5		
65	A	1.0	14.5	14.5	215	246	234	0.15	0.69	4		
66 (2/3)	A	1.0	12.0	14.8	198	246	232	0.13	0.64	5	249	5.9±0.5
67	A	0.9	11.3	13.8	215	243	227	0.13	0.59	4		5.4±0.0
68	A	1.0	13.7	13.7	224	254	228	0.15	0.67	4		
69	A	0.9	14.3	15.3	202	247	226	0.14	0.67	4		
70 (2/4)	B	1.1	15.1	15.1	203	252	242	0.17	0.83	4		
71	B	1.1	13.5	13.5	227	246	222	0.14	0.62	5		
72	A	1.1	15.8	15.8	175	239	217	0.17	0.83	5		
73	A	0.9	16.7	16.7	223	246	221	0.14	0.73	4		
74 (2/5)	B	1.1	16.0	16.0	175	237	227	0.18	0.91	4		4.7±0.4
75	B	1.1	14.0	14.0	167	247	218	0.16	0.73	4	246	5.7±0.6
76	B	1.1	13.4	14.2	227	240	230	0.17	0.79	4	246	5.2±0.6
77	B	1.1	14.4	14.4	219	229	225	0.16	0.76	1	246	5.1±0.0
78 (2/6)	B	1.4	15.4	15.4	178	248	206	0.21	1.05	1	252	5.4±0.4
79	B	1.4	14.8	14.8	203	250	209	0.21	0.99	1	252	5.7±0.4
80	B	1.3	14.5	14.5	196	217	206	0.20	0.91	3	252	5.3±0.3
81	B	1.6	13.7	13.7	208	255	233	0.24	1.05	1	252	5.4±0.3
82 (2/7)	B	1.4	14.2	14.2	204	240	233	0.19	1.05	1	252	5.5±0.4

Note: The first frame was taken at 18:00, January 17, 2002. The time increment is 6 h. Significant wave height,  $H_s$ , and peak period,  $T_{p,ses}$ , are calculated from the surface elevation spectra,  $S_\eta(\omega)$ .  $T_{p,bovs}$  is the peak period found in the bottom orbital velocity spectra,  $S_u(\omega)$ .  $U_{rms}$  and  $d_0$  are, respectively, the root-mean-square bottom orbital velocity and orbital diameter. Ripple orientation is the bearing of the line that is perpendicular to the ripple crests. The 95% confidence intervals for ripple spacing measurements are also shown. Bold rows are four local storms.

Wave types: A = uni-modal swells; B = dual-modal, swells dominant; C = dual-modal, wind-wave dominant.

Ripple types: 1 = sharp crest vortex ripples, 2-D; 2 = brick-pattern ripples, 3-D; 3 = sharp crest, bifurcating ripples, 3-D; 4 = smooth and round crest ripples, 3-D; 5 = flat bed.

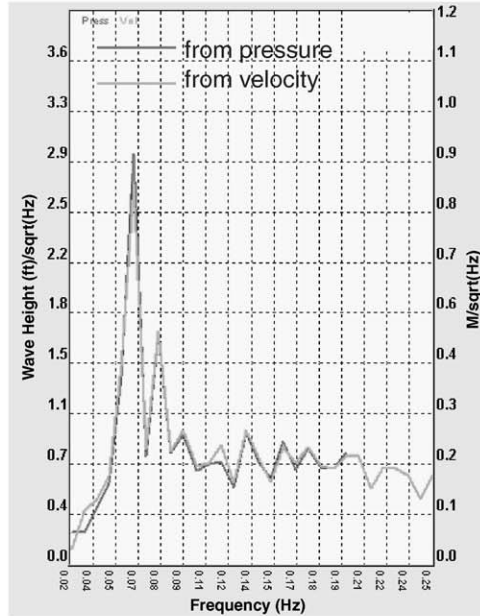
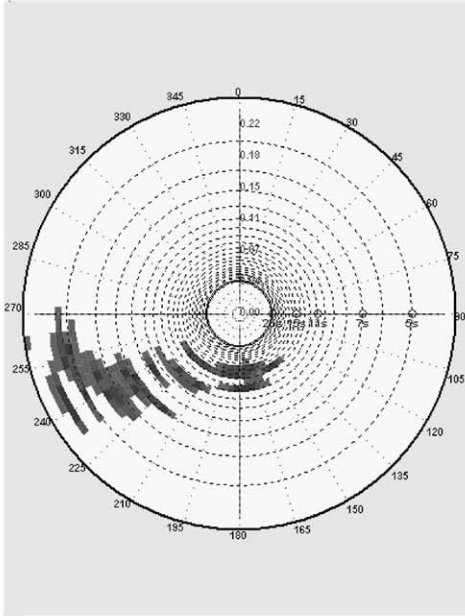
Wave heights and wave periods are calculated from the zeroth and first moments ( $m_0, m_1$ ) of the frequency spectra:

$$m_0 = \int_{\omega_1}^{\omega_2} S_\eta(\omega) d\omega, \tag{1}$$

$$m_1 = \int_{\omega_1}^{\omega_2} \omega S_\eta(\omega) d\omega, \tag{2}$$

where  $\omega$  is the radial frequency and  $S_\eta(\omega)$  is the surface elevation spectrum.  $\omega_1$  and  $\omega_2$  are, respectively, the minimum and maximum frequencies

18:00, January 17, 2002 (Frame 1)



18:00, January 28, 2002 (Frame 45)

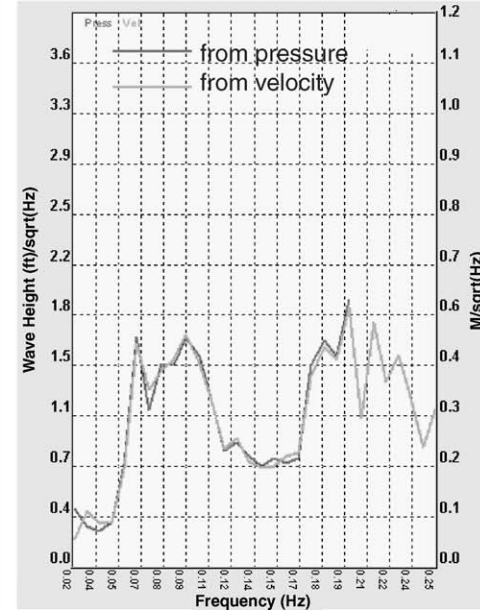
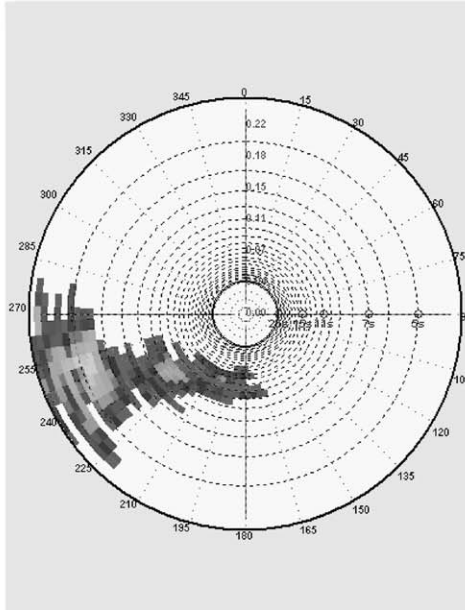


Fig. 4. Graphic output from RDI's WaveView analysis of ADCP data showing the directional spectra of two types of wave conditions—uni-modal (top panel) and bi-modal (bottom panel). It also shows that long-period swells primarily come from the south, and short-period wind waves mainly come from WSW. The two lines in the frequency spectra, essentially identical, are, respectively, from pressure (darker line) and beam velocities (lighter line).

of the spectra. The significant wave height is  $H_s = 4.004\sqrt{m_0}$ , and the mean wave period is  $T = 2\pi m_0/m_1$  (Massel, 1996). Peak wave periods,  $T_{p,ses}$ , often used in bed shear stress calculations, are obtained from the surface elevation spectra where the energy density is the maximum. Dominant wave directions are obtained in the same fashion, from the directional spectra. Since bed shear stress is more directly associated with near-bed orbital velocity than with wave height, frequency spectra of the near-bed orbital velocity,  $S_u(\omega)$ , are calculated from the surface elevation spectra,  $S_\eta(\omega)$ :

$$S_u(\omega) = \frac{\omega^2}{\sinh^2(kh)} S_\eta(\omega), \quad (3)$$

where  $h$  is the water depth,  $k$  is the wave number that is related to  $\omega$  by the dispersion relation  $\omega^2 = gk \tanh(kh)$ , and  $g$  is the gravity acceleration. The root-mean-square (RMS) as well as the significant near-bed orbital velocity are also computed with the moment method (Massel, 1996):

$$u_{rms}^2 = \int_{\omega_1}^{\omega_2} S_u(\omega) d\omega, \quad (4)$$

$$A_{rms} = \frac{u_{rms}}{\omega}, \quad (5)$$

$$A_{sig} = \sqrt{2}A_{rms}. \quad (6)$$

The near-bed orbital diameter,  $d_0$ , is twice the orbital semi-excursion  $A_{rms}$ , or  $d_0 = 2A_{rms}$ .

Fig. 5 shows the frequency spectrum of both surface elevation and near-bed orbital velocity of two typical wave conditions during the deployment. Because shorter waves attenuate with water depth more rapidly than longer waves, the spectral characteristics of the near-bed orbital velocity spectrum can be very different than the surface elevation spectrum. During a local wind storm (January 23, 2002) for instance, the peak wave period measured from the surface elevation spectra,  $T_{p,ses}$ , was 8 s (Fig. 5). This is substantially smaller than the peak period observed from the bottom orbital velocity spectra,  $T_{p,bovs}$ , of 18 s. In such cases of poly-modal wave spectra, which are not uncommon in field data, one should be cautious in using the peak period  $T_{p,ses}$  for

estimation of bed shear stress, orbital diameter  $d_0$ , and other bottom boundary layer parameters. Also plotted in Fig. 5 are the near-bed orbital velocities derived from three different methods: (1) using linear wave theory and the peak parameters of the surface elevation spectra; (2) using Eq. (3); and (3) calculating the orbital velocity from the first-bin ADCP velocity measurements. Occasionally, the values from method 1 are equal to, or slightly greater than, the values from the other two methods, but the majority of the values from method 1 are significantly smaller than the other two counterparts.

## 4. Results

### 4.1. Waves and currents

Three typical sea states were observed during the 20 days when sand ripples on the sea floor were recorded: (1) long-period (12–18 s) swells generally from the south; (2) short-period (5–10 s) wind waves that are locally generated and mostly from the west-southwest (WSW); and (3) a mixture of the two. Fig. 6 plots the time series of energy spectrum computed from the ADCP data. Five separate swell systems, whose wave height ranges from 0.8 to 1.2 m, can be clearly identified. Because swells with longer periods also propagate faster, the dispersion relation ( $\omega^2 = gk \tanh(kh)$ ) that is clearly shown in Fig. 6 implies that this group of swells originated roughly 8000 km away and needed 6.5 days of propagation to reach the site. In addition to the swells, there were one major and two minor local storms during the 20-day period. The strength of wind waves is mainly dependent on wind speed, duration, and direction. The major wind waves that occurred on January 22–23 were caused by a 10 m/s westerly wind that lasted more than 6 h. In contrast, the wind speed reached more than 10 m/s on January 24, but because it was northeasterly, the wave height at the site was much smaller than that in the previous day.

The three sea states are re-classified into four wave types for the purpose of correlating with ripple types described in the next section. The four

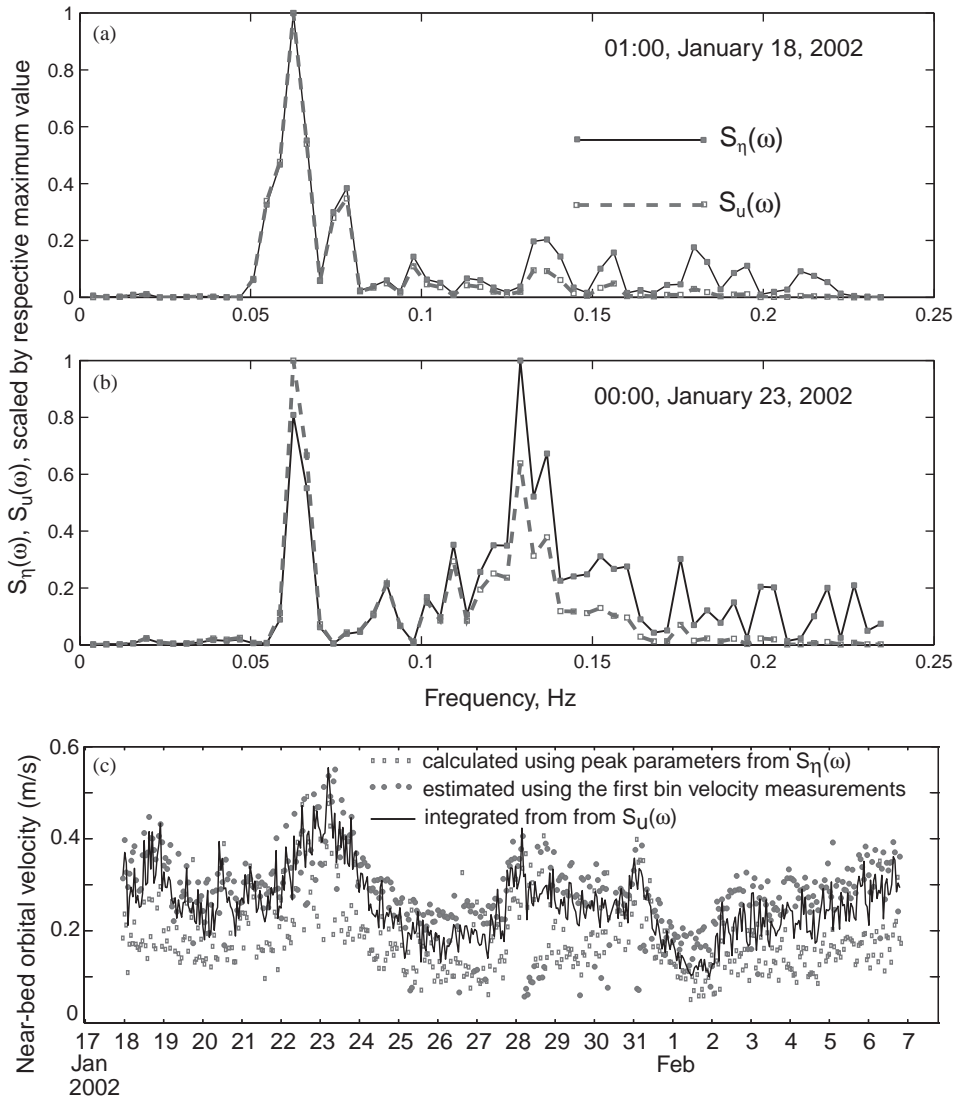


Fig. 5. Panels (a) and (b) show, respectively, the frequency spectra of surface elevation,  $S_{\eta}(\omega)$ , and bottom orbital velocity,  $S_u(\omega)$ , for two different wave types. For wave type C (bi-modal, wind-wave dominant), peak parameters obtained from  $S_{\eta}(\omega)$  can be very different from that derived from  $S_u(\omega)$ . Using the peak parameters of  $S_{\eta}(\omega)$  may result in underestimation of near-bed orbital velocity, shown in panel (c).

types are identified from the frequency wave spectra: (A) uni-modal, swells only; (B) bi-modal, swells dominant; (C) bi-modal, wind-wave dominant; and (D) uni-modal, wind waves only. Because long-period swells always existed in the area during the 20-day period, wave type D was never encountered. The wave types corresponding to the times of the 82 video frames are listed in

**Table 1.** Significant wave heights,  $H_s$ , and peak wave periods,  $T_{p,ses}$ , each an average over the 2 h prior to the video frame, as well as the bottom orbital semi-excursion  $A_{rms}$  are listed in **Table 1** and plotted in **Fig. 7**. Among the 82 video frames, wave type B was most dominant with 43 occurrences (52%). There were 18 occurrences of wave type A (22%) and 21 occurrences of wave type C

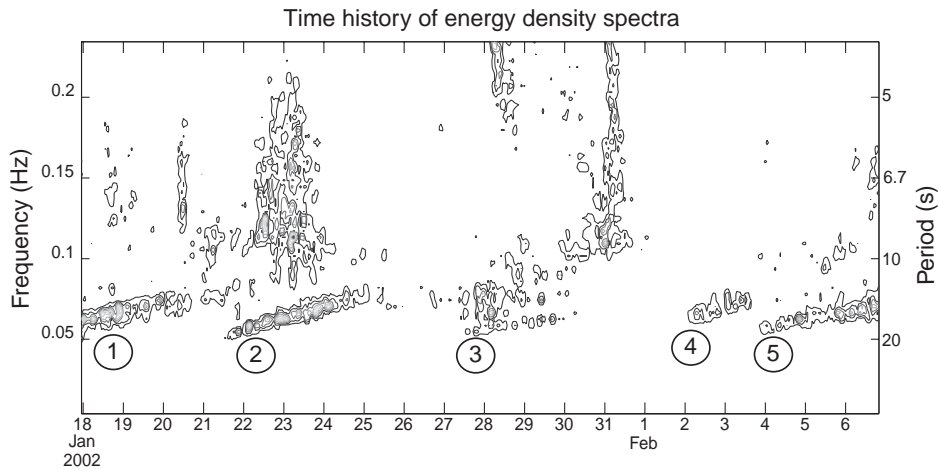


Fig. 6. A contour plot showing the time history of wave spectra at the site. The five swell systems are numbered (number in a circle). While local wind waves (periods of 5–10 s) only existed sporadically, the long-period swells (periods of 12–18 s) came from a distance almost continuously. The dispersive property of the swells suggests they originated 8000 km away.

(26%). Among the 18 occurrences of type A waves, 12 of them were low energy conditions (also see Table 2 in Section 4.2). At the opposite end of the spectrum, 18 of 21 type C waves occurred during the periods of high wave energy.

Alongshore current dominated the lower part of the water column. The semi-major axis of the current (the first ADCP bin,  $\sim 2.7$  m above bed) ellipse was 2.5 times the semi-minor axis and had the azimuth of  $126^\circ$ , which was almost parallel to the coastline. Both tidal and subtidal currents were fairly weak ( $< 10$  cm/s). The subtidal currents were predominantly equatorward, resulting in a down-coast current at a mean speed of 2.5 cm/s. The tidal current during spring tide was more than two times that during neap tide, but the maximum tidal current was still generally less than 10 cm/s. There was no near-bed current measurement on the tripod at HB03, but measurement of currents 60 cm above the bed by an acoustic Doppler velocimeter (ADV) on the HB05 tripod in 25 m showed very similar current patterns. Therefore, it is reasonable to assume that the near-bed currents at HB03 had the same patterns as the first-bin measurements, only with smaller magnitudes. Except for several calm periods, the mean currents were significantly weaker than the wave orbital velocity. During the 20-day deployment,  $\sim 90\%$  of calculated RMS near-bed orbital velocity were

equal to or greater than 13 cm/s,  $\sim 70\%$  were greater than 15 cm/s, and 30% were greater than 20 cm/s. The average orbital velocity was 18 cm/s and the maximum reached 50 cm/s during the January 23 storm. Since the wave friction factor is normally more than one order of magnitude greater than the current drag coefficient, the bed shear stress due to mean currents is much smaller than due to waves of the same velocity. Employing the empirical method in Soulsby (1997), the bed shear stress from a 10 cm/s mean current is only 15% of that caused by waves (10 s period) with a 10 cm/s orbital velocity. Using the average value of the mean currents, 6 cm/s, its shear stress is  $8.76 \times 10^{-3}$  N/m<sup>2</sup>. This is less than 2% of the shear stress ( $0.53$  N/m<sup>2</sup>) caused by the average wave orbital velocity of 18 cm/s. Because this paper mainly focuses on bed shear stress and sediment transport, the weak mean currents are omitted in the ensuing discussions.

#### 4.2. Ripple types (plan-view shapes)

Because the height of the sand ripples could not be measured from the video images, ripple types are determined by the spacing of the ripples and their plan-view appearance. This approach of ripple classification has been applied in other studies (Boyd et al., 1988; Osborne and Vincent,

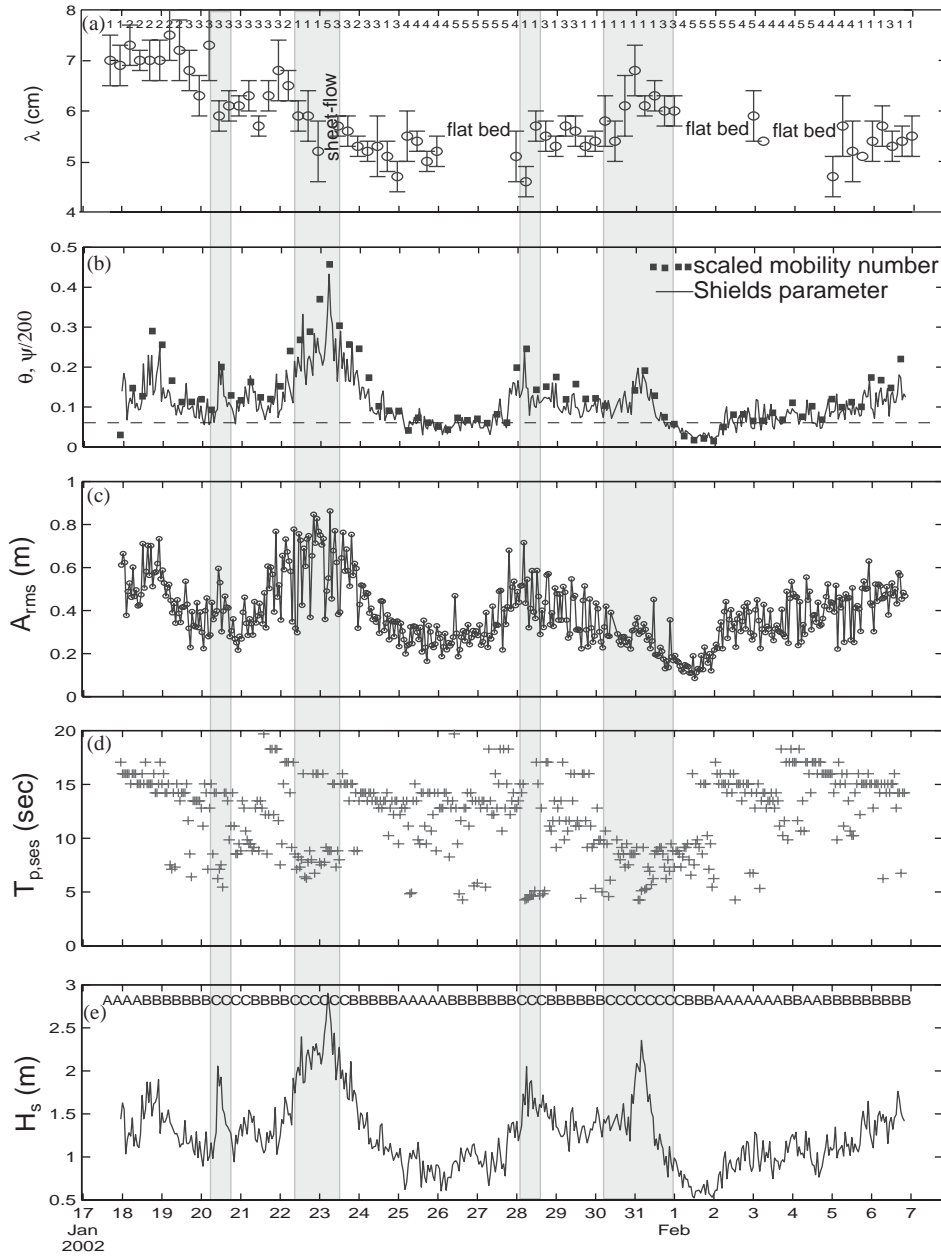


Fig. 7. Time-series plots showing (a) ripple spacing  $\lambda$  and ripple types; (b) Shields parameter  $\theta$ , with the dashed line designating the critical Shields parameter for fine sands, and the mobility number  $\psi$ , scaled by 200; (c) RMS bottom orbital semi-diameter  $A_{rms}$ , calculated in Eq. (4); (d) peak wave period,  $T_{p,ses}$ , obtained from surface elevation spectra; and (e) significant wave height  $H_s$  and the three wave types. The grayed vertical bars indicate the four local storms, also highlighted in Table 1.

1993). The observed bedforms during the 20-day period are classified into five categories (Fig. 8): (1) sharp-crested, two-dimensional (2-D) ripples; (2)

sharp-crested, brick-pattern, 3-D ripples; (3) bifurcated, 3-D ripples; and (4) round-crested, smooth, 3-D shallow ripples. If there are no

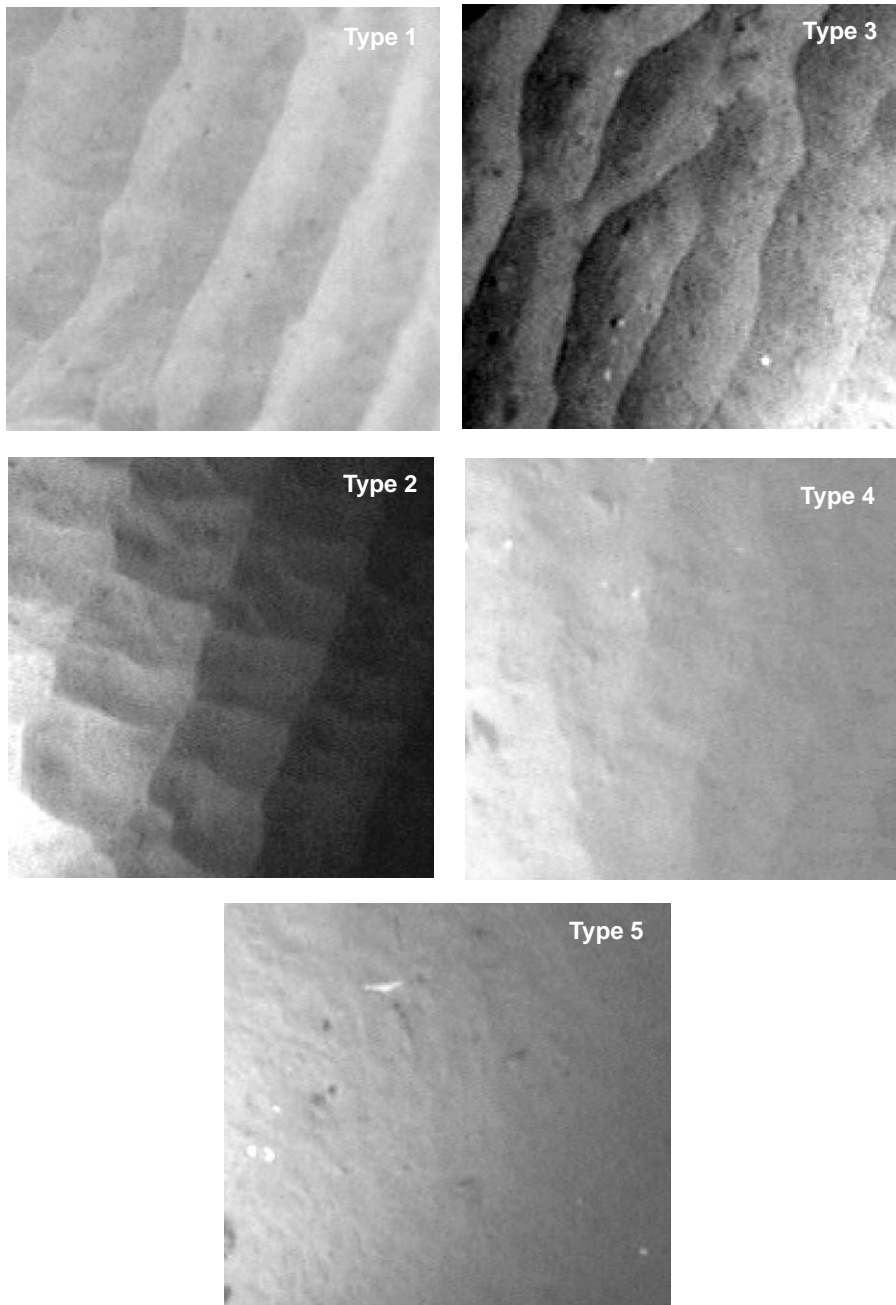


Fig. 8. Examples of ripple types: (1) sharp-crested vortex, 2-D; (2) sharp-crested, brick-pattern, 3-D; (3) sharp-crested, bifurcating, 3-D; (4) smooth- and round-crested, 3-D; (5) flat bed.

bedforms on the sea floor, it is classified as bedform type (5) flat bed. Two independent assessments of bedform types were made and they

agreed for most of the frames. For those frames with two different classifications, the differences were reconciled and a final classification was

determined. Although great care was exercised in this classifying procedure, there is inevitably some subjectivity involved simply because of the “human factor”. Table 1 lists the characterization of measured waves and sand ripples in 82 digital video frames. Each image represents the typical ripple characteristics observed in a 90-s video segment recorded every 6 h.

It was seen in the video that bedload transport occurred in association with ripple types 1, 2, and 3. Oscillatory movements of sand grains were clearly observed on these types of ripples, especially on the ripple crest. For type 4 ripples no such movement of sand grains was observed. Sleath (1984) suggested that sand ripples become progressively more 3-D (types 2 and 3) as the bedload sediment transport rate increases, but this trend was not observed in our video data. In fact, 3-D ripples, especially type 3, tended to become more 2-D as the sediment transport increased. The joint frequency distribution of wave and ripple types is shown in Table 2. Correlation between wave and ripple types can be summarized as follows. Firstly, long-period swells dominated the sea state during the 20-day observation. Among 82 total sea states 61 were either swells only (type A) or swells dominant (type B). All bedform types existed in swell-dominated environments. Secondly, type C waves were highly associated with ripple types 1 and 3 (two of the “high energy” ripples), whereas type A waves were highly associated with “low

energy ripples” (types 4 and 5). In other words, the sharp-crested vortex ripples (2-D or 3-D) are mainly created under the sporadic, shorter-period wind waves although long-period swells are constantly present. Thirdly, brick-pattern ripples (type 2) were observed in only eight video frames, all in swell-dominated conditions (wave types A and B). Previous observations of this type of sand ripples have prompted different attempts to explain how this special pattern is formed. Sleath (1984) theorized that the brick-pattern ripples are formed under relatively low sediment transport rate, and the pattern is a more stable configuration than even 2-D ripples. Allen (1982) suggested that the two orthogonal ripples (called bridges and transverse crests in Sleath, 1984) are related, respectively, to “two sets of waves that have been generated by obstacles acting upon a single parent wave set as it marched toward shore”. These mechanisms do not appear to be consistent with the observations, but the eight observations presented here are too limited to confirm or reject any hypothesis. In all eight cases, the two orthogonal ripple sets already existed at the beginning of the 90-s video; therefore, it is unknown whether one set was formed a head of the other. One set of ripples was always clearly dominant than the other. The brick-pattern ripples were observed early in the deployment (Table 1 and Fig. 7) but never reoccurred, even under similar wave conditions later in the deployment.

Table 2  
Joint frequency table of the wave types and ripple types

	Wave types			Total
	A	B	C	
<i>Ripple types</i>				
1	(2.4%) 2	(12.2%) 10	(12.2%) 10	(26.9%) 22
2	(2.4%) 2	(7.3%) 6	0	(9.7%) 8
3	0	(14.6%) 12	(11.0%) 9	(25.6%) 21
4	(12.2%) 10	(6.1%) 5	(1.2%) 1	(19.5%) 16
5	(4.9%) 4	(12.2%) 10	(1.2%) 1	(18.3%) 15
Total	(21.9%) 18	(52.4%) 43	(25.6%) 21	82

Note: Both the number of occurrences and percentages are listed.

Wave types: A = uni-modal swells; B = dual-modal, swells dominant; C = dual-modal, wind-wave dominant.

Ripple types: 1 = sharp crest vortex ripples, 2-D; 2 = brick-pattern ripples, 3-D; 3 = sharp crest, bifurcating ripples, 3-D; 4 = smooth and round crest ripples, 3-D; 5 = flat bed.

### 4.3. Ripple spacing

The sand ripples described in this paper are predominantly wave ripples; thus, the ripple properties ought to be related to the wave characteristics, such as wave heights, periods, directions, directional spreading, and the like (Boyd et al., 1988; Osborne and Vincent, 1993; Amos et al., 1988). These relations, however, are not found in the ripple data presented here. In Fig. 7, the ripple spacing,  $\lambda$ , measured from the 82 video frames is plotted along with the significant wave height  $H_s$ , peak wave period  $T_p$ , bottom orbital semi-excursion  $A_{rms}$ , and Shields parameter,  $\theta$  ( $= \tau_b / (\rho_s - \rho)gd_{50}$ , where  $\tau_b$  is the bed shear stress,  $\rho_s$  and  $\rho$  are sediment and water densities,  $g$  is the gravitational acceleration, and  $d_{50}$  is the median grain size). Wave and ripple types (see Table 1 and Fig. 8 for definition) are also shown, respectively, in panel (a) and panel (e). The ripple spacing values are very small, between 4.5 and 7.5 cm. This is partially due to the small grain size of fine sands at the site: the  $D_{50}$  value of 92  $\mu\text{m}$  is smaller than the grain sizes in most published field studies (Dingler, 1974; Miller and Komar, 1980; Amos et al., 1988; Osborne and Vincent, 1993; Jette and Hanes, 1996; Traykovski et al., 1999). Inman (1957) and Boyd et al. (1988) presented ripples of fine sands (120 and 110  $\mu\text{m}$ , respectively) in similar shelf environments (10 and 16 m water depth, respectively). They both observed ripples with spacing as small as 6 cm, but they also observed ripples greater than 20 cm, almost three times the largest ripples in the data presented here. The largest ripples were recorded at the beginning of the deployment (Fig. 7a) under type A (swells only) and type B (bi-modal, swell dominant) wave conditions. However, there is no apparent correlation between ripple spacing  $\lambda$  and any of the wave parameters (wave type,  $H_s$ ,  $T_p$ , and  $A_{rms}$ ). The only identifiable relation in Fig. 7 is between ripple spacing  $\lambda$  and Shields parameter  $\theta$ —there are sand ripples on the sea floor when  $\theta$  is greater than 0.06–0.07 and the sea floor becomes a flat bed when  $\theta$  is less than this value. This critical value of Shields parameter is almost 1.5 times the critical value in a Shields parameter curve (e.g., Nielsen,

1992; Soulsby, 1997) for the grain size of  $D_{50} = 92 \mu\text{m}$ .

The lack of correlation between ripple spacing  $\lambda$  and waves suggests the sand ripples recorded on the San Pedro shelf fall into the category of anorbital ripples (Clifton and Dingler, 1984). This is also supported by the relations illustrated in Fig. 9. The scatter plot of ripple spacing  $\lambda$  and orbital diameter  $d_0$ , both scaled by the median grain size  $D_{50}$ , shows that all but one observed ripples from this study have a  $d_0/D_{50}$  ratio greater than 5000, a limit that separates anorbital from orbital or suborbital ripples (Clifton and Dingler, 1984; Traykovski et al., 1999). This is not a surprise because most field-observed sand ripples (e.g., Inman, 1957; Dingler, 1974; Boyd et al., 1988; Amos et al., 1988) are also primarily anorbital and suborbital. Compared with other field data plotted in Fig. 9, the  $\lambda$  of the ripples from San Pedro shelf are not only smaller than other ripples but also much less variable. This may be partially due to the fact that all the observations on the San Pedro shelf were made at a single location. Except Boyd et al. (1988), all other field data consist of measurements from different locations with different grain sizes in different water depths. Some of the variability in ripple spacing in Fig. 7 could have been caused by temporal variation of grain size, but this cannot be verified due to the lack of a time-series measurements of grain size. Nielsen's (1981) empirical formulation with the mobility number  $\psi$ ,

$$\frac{\lambda}{A} = \exp\left(\frac{693 - 0.37 \ln^8 \psi}{1000 + 0.75 \ln^7 \psi}\right) \quad (7)$$

which was obtained by synthesizing field results by Inman (1957), Dingler (1974), and Miller and Komar (1980), appears to overestimate the ripple spacing for the San Pedro shelf ripples. A linear, least-square fit in the logarithmic plot in Fig. 9 produces a simpler formula:

$$\frac{\lambda}{A} = 0.83\psi^{-0.54} \quad (8)$$

A more straightforward relation for anorbital ripples is

$$\lambda = cD_{50}, \quad (9)$$

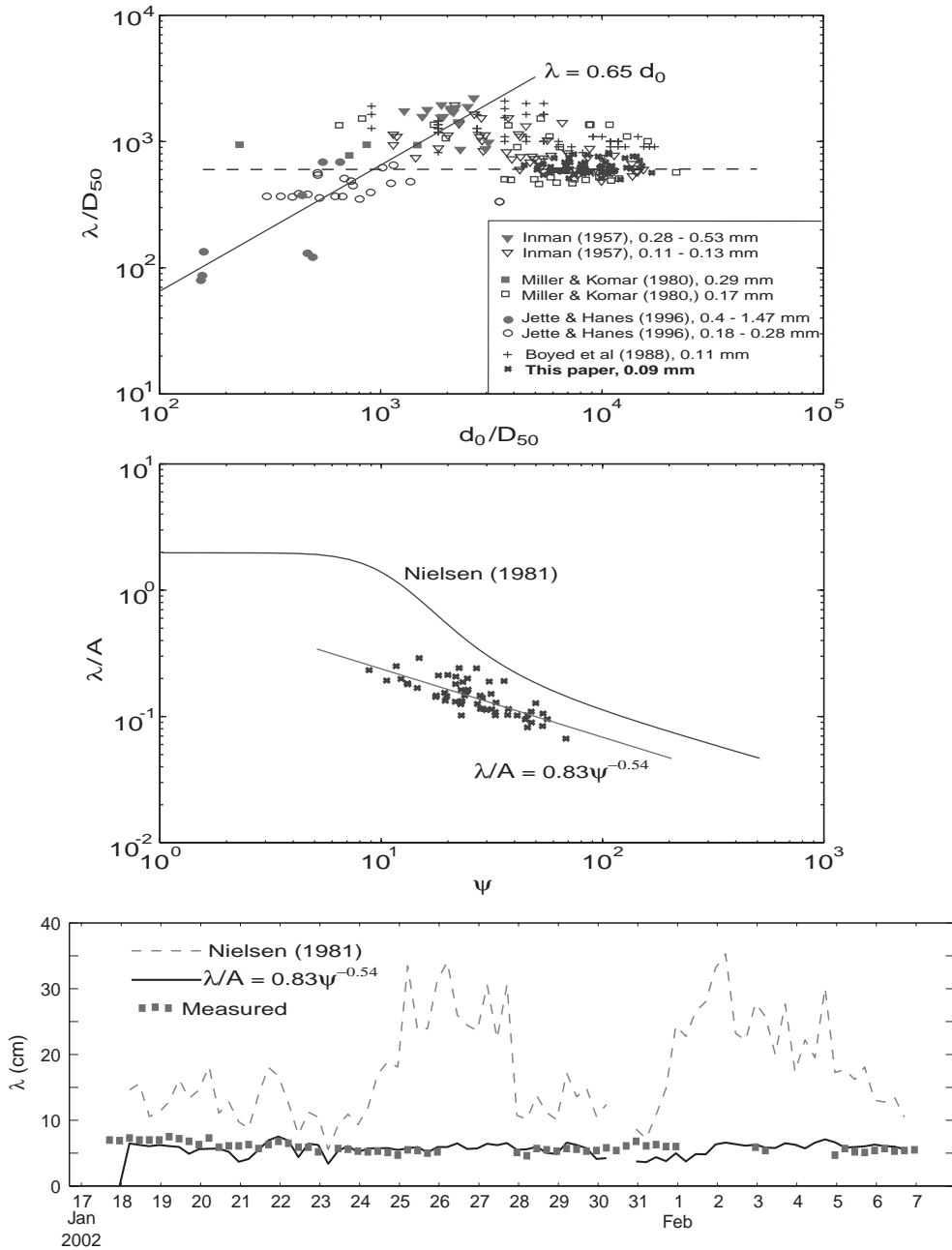


Fig. 9. (a) A log–log plot of ripple spacing  $\lambda$  vs. bottom orbital diameter  $d_0$ , both scaled by the median grain size  $D_{50}$ , from five field studies. The horizontal dashed line represents  $\lambda = 600D_{50}$ . (b) A plot of  $\lambda/A_{rms}$  as a function of Nielsen's (1981) mobility number  $\psi$ . The solid curve is Nielsen's empirical formula for field ripple data. The dashed line is the least-square best fit for the data from this paper. (c) A time-series plot of measured ripple spacing  $\lambda$  as well as calculated  $\lambda$  using the two formula in (b).

where  $c$  is a constant that ranges between 400 and 600 (Clifton and Dingler, 1984; Wiberg and Harris, 1994). For the San Pedro shelf data, the values of  $c$  varies between 500 and 700 and can be best represented by  $c = 600$  (the dashed line in Fig. 9).

Boyd et al. (1988) postulated, after analyzing ripple data from Inman (1957), Dingler (1974), Miller and Komar (1980), and their experiment on the Nova Scotia shelf, that there might be a lower ripple spacing limit of 6 cm in open-ocean environments. For anorbital ripples, where the ripple spacing  $\lambda$  is scaled by the grain size (e.g.,  $\lambda = 600D_{50}$ ), it is only logical to suggest that the lower limit of ripple spacing should also be scaled by the grain size. The ratio of  $\lambda_{\min}$  to  $D_{50}$  in Boyd et al. (1988) is 545. The smallest ripple on San Pedro shelf has  $\lambda_{\min} = 4.6$  cm, thus the ratio  $\lambda_{\min}/D_{50}$  is 500, a slightly smaller value. Whether this relation of scaling the lower limit of anorbital ripple spacing is valid or just coincidental will need to be tested with more field data. It is interesting to

note, however, that this ratio is also close to Wiberg and Harris's (1994) 535, a value determined from a combined field and laboratory data.

#### 4.4. Ripple orientation

Orientations of wave-generated ripples under monochromatic waves should directly correspond to wave direction (Carstens et al., 1969; Mogridge and Kamphuis, 1972). This correspondence may also apply to a well-defined uni-modal spectral wave train (wave type A or D) (Boyd et al., 1988; Traykovski et al., 1999). Ripple orientations under poly-modal, multi-directional spectral waves are not well known because simultaneous measurements of such waves and ripples are scarce. Fig. 10 shows ripple orientations defined as the bearing of a line perpendicular to the ripple crests. Also shown in Fig. 10 are wave types, peak wave directions taken from the directional wave spectra, and the azimuth of the orbital velocity that are estimated from the scatter plot of the two

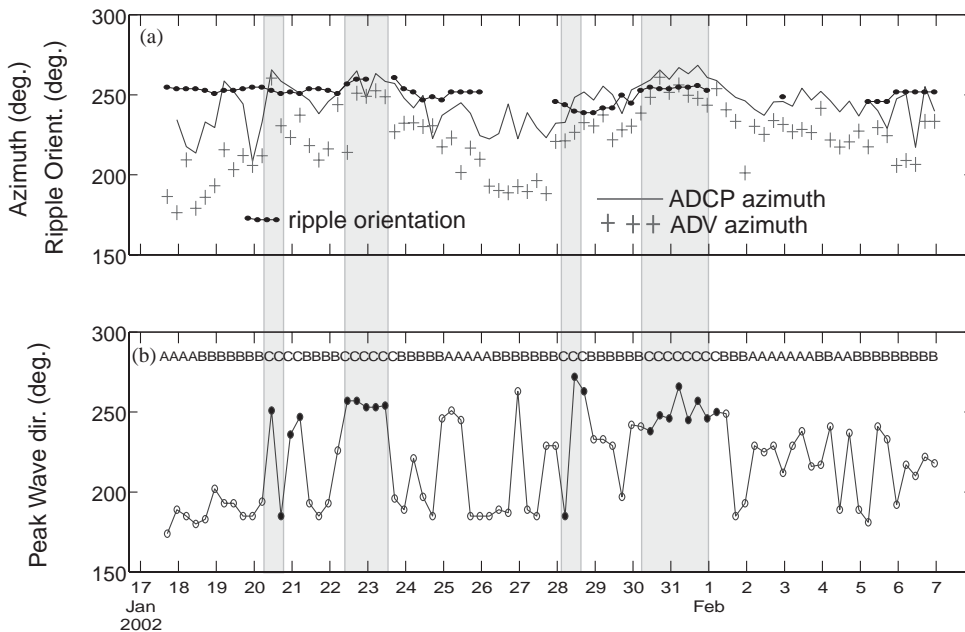


Fig. 10. (a) Time-series plots of the azimuth of the velocity ellipses from the ADCP at HB03 and the ADV at HB05 stations. The first bin of the ADCP is about 2.7 m above sea floor; the ADV measures velocity at 60 cm above sea floor. Also plotted in this panel is the measured ripple orientation, defined as the bearing of a line perpendicular to the ripple crests. (b) Plots of wave types and time series of peak wave direction. Directions of type C waves are highlighted with filled circles. The grayed vertical bars indicate the four local storms, also highlighted in Table 1.

horizontal velocity components. The azimuth is estimated from the first bin of ADCP data, which is  $\sim 2.7$  m above the bed, and a near-bed (60 cm above the bed) ADV on a tripod at HB05 (1.8 km offshore of HB03). The difference between the ADCP azimuth and ADV azimuth is due to the fact that the ADV is in deeper water (24 m) than the first bin of the ADCP ( $\sim 12$  m). Deeper water filters out the “noise” from higher frequency waves that normally have broader directional spreading; thus, the ADV azimuth displays a larger magnitude of change over time but less high frequency “noise”. Ripple orientations varied between  $240^\circ$  and  $260^\circ$  during the 20-day period. The  $20^\circ$  range is much smaller than either the azimuth’s variation ( $40^\circ$  range for ADCP and  $90^\circ$  for ADV) or the peak wave directions that varied between  $180^\circ$  and  $270^\circ$ .

For swell-dominated waves (types A and B) that mainly come from the south, the ripple orientations are in a large oblique angle with the wave direction, and this angle changes over time. For instance, during January 17–19 (wave type A), the difference between wave direction and ripple orientation is  $60$ – $70^\circ$ . The ripple orientation, peak wave direction, and azimuth only lined up during the two strongest storms on January 22–23 and January 30–31. All three had a value of around  $250$ – $260^\circ$  for 24–30 h. Duration of the storm also seems to be a factor. For the two brief storms on January 20 and 28 (both lasted less than 12 h), the ripple orientation was not aligned with the waves as during the longer storms. This indicates that a time-lag exists between wave forcing and ripple response, although there is not enough data to suggest the length of the time-lag. The eccentricities, defined as the ratio of the semi-minor axis to the semi-major axis of the ellipses in the scatter plots (not shown), during these storms (wave type C) were as low as 0.4, indicating the dominance of wind waves with narrow directional spreading. In contrast, the eccentricities were much higher (around 0.7) for wave types A and B. During these swell-dominated wave conditions (especially wave type B), the peak wave directions that are directly read from the directional spectra do not reflect the orientation of the near-bed orbital flows that are driving the bed shear stress and sediment transport.

## 5. Discussion

Most published studies on sand ripples and their interactions with surface waves assume that waves are monochromatic or uni-modal in frequency spectrum and come in one direction. In the field, however, waves are more often than not poly-modal in frequency and multi-directional (Miller and Komar, 1980; Karl et al., 1980). As suggested in previous sections, some empirical ripple-wave relations developed from simple lab or field wave conditions may not be used for the poly-modal, multi-directional wave environments.

### 5.1. Waves of poly-modal frequency spectrum

The geometry of sand ripples is determined by the physical properties of sand grains (median grain size  $D_{50}$ , density  $\rho$ , etc.) and wave forcing (near-bed orbital velocity and orbital diameter  $d_0$ ). In a monochromatic or uni-modal spectral wave environment, the orbital diameter can be easily estimated from the significant wave height  $H_s$  and peak wave frequency  $\omega_p$  (Grant and Madsen, 1982; Soulsby, 1987; Nielsen, 1992), both of which are common measurements in most laboratory and field studies. Although the peak frequency of the near-bed orbital velocity may be slightly lower than that of the surface waves depending on water depth, measures have been developed to account for this problem (Soulsby, 1987). Under a poly-modal wave spectrum, however, it could become erroneous if the  $H_s$  and  $\omega_p$  of surface waves are used to compute orbital diameter because the peak frequency of the near-bed orbital velocity could be very different from that of the surface waves (see Fig. 5).

Given the significant wave heights and peak wave periods from a measured wave spectrum, the RMS orbital diameter can be estimated as if it is for a monochromatic wave in linear wave theory (Soulsby, 1987). Such calculated orbital diameters are plotted in Fig. 11 against the RMS orbital diameter estimated from the near-bed orbital velocity spectra (Massel, 1996). The former is systematically higher (about 20%) when the peak wave periods found from both the surface wave spectra and bottom orbital velocity spectra are the same. Potential sources of this discrepancy are not

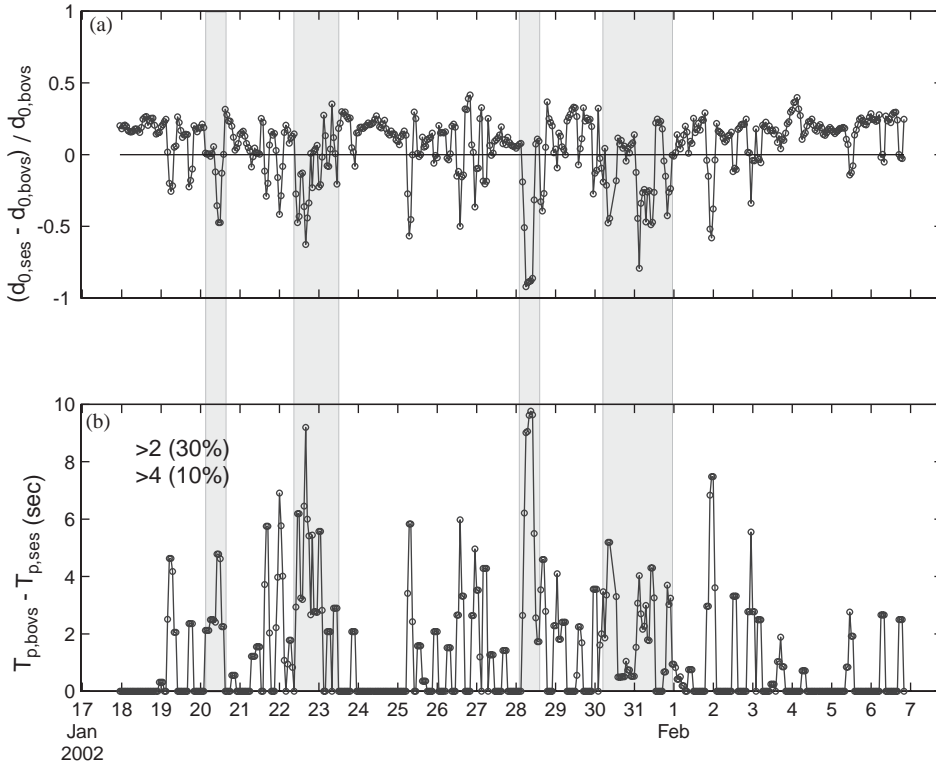


Fig. 11. Time-series plots of (a) difference of bottom orbital diameters calculated using the peak parameters of  $S_\eta(\omega)$ , the surface elevation spectra ( $d_{0,ses}$ ) and that using  $S_u(\omega)$ , the bottom orbital velocity spectra ( $d_{0,bovs}$ ); and (b) difference of peak wave periods  $T_{0,ses}$  and  $T_{0,bovs}$ . In the 20-day period, the difference of peak period was above 4 s for 10% of the time, and 2 s for 30% of time. This leads to significant underestimation of bottom orbital velocity and diameter if peak parameters from  $S_\eta(\omega)$  were used. The grayed vertical bars indicate the four local storms, also highlighted in Table 1.

pursued here, but it does not affect the validity of the aforementioned arguments: in a type C wave environment (poly-modal spectra with a peak at the higher frequency) using the significant wave height  $H_s$  and peak wave frequency  $\omega_p$  in the linear wave theory approach to estimate the orbital diameter  $d_0$  could result in significant underestimations. This is highlighted in four grayed time-bands in Fig. 11 when both swells and wind waves were present but the latter was more dominant in wave energy (Fig. 7). On January 28, for instance, a local wind storm passed by and sea states were dominated by 4–6 s short-period waves. The difference between  $T_{p,ses}$  and  $T_{p,bovs}$  was as high as 10 s and the underestimation was 90%. The overall difference between the two peak periods was greater than 2 s 30% of the time, and

4 s 10% of the time. During those times, the underestimations were between 10% and 25%.

### 5.2. Poly-modal, multi-directional waves

This discussion has so far been limited to poly-modal but uni-directional wave conditions. In fact, the majority of published studies on ripple-wave relations are also for uni-directional waves, if not monochromatic or uni-modal spectral waves. Karl (1976) and Drake et al. (1985) observed crossing ripples on the shelf of northern San Pedro Bay and attributed the two sets of ripples to long-period swells (for larger ripples) and short-period wind waves (for smaller ripples) from almost perpendicular directions. Despite frequent poly-modal, multi-directional wave conditions during this

investigation, there are no ripple images from the video footage that indicate the coexistence of two or more sets of ripples. In order to have two coexisting sets of ripples of different sizes at the same place, ripples must be orbital ripples (Clifton and Dingler, 1984). It is difficult to observe orbital ripples in field experiments due to high value of  $d_0/D_{50}$  ratio, especially on a seabed comprised of fine sands as described in this paper. At sites where orbital ripples are possible, ripples of different sizes are more likely to be formed one after another (probably the smaller ripples after the larger ones) than to be formed simultaneously.

Fig. 12 demonstrates (in a simplified fashion using monochromatic instead of spectral waves) the situation of poly-modal, multi-directional wave conditions. Both wave trains have their bottom orbital velocity in the form of  $u = u_0 \cos(\omega t + \theta)$ , where  $u_0$  is the amplitude,  $\omega$  is the radial frequency, and  $\theta$  is an arbitrary phase angle that is irrelevant to the discussion here. Plots of the orthogonal velocity components ( $U$ ,  $V$ ), the speed ( $W$ ), and the water particle tracks from the linear additions of the two wave trains show that the summed bottom orbital velocity is strongly dependent on the angle between the two wave trains. Ignoring the directions of the wave trains, the RMS bottom orbital velocity under the two wave trains would be  $\sqrt{0.5(u_{01}^2 + u_{02}^2)} = 16.5$  cm/s. As the angle between the two wave trains increases, the summed RMS bottom orbital velocity, which equals the semi-major axis of the principal components, decreases: 16.2 cm/s for a smaller angle ( $\frac{\pi}{7}$ ) compared to 14.4 cm/s for a larger angle ( $\frac{3\pi}{12}$ ). These arguments concerning orbital velocity should also apply to orbital diameter,  $d_0$ , because of  $d_0 = 2u_{\text{rms}}/\omega$ . The water particles under the combined wave conditions have a rather complicated oscillating track that also dramatically changes with the angle between the two wave trains. In many of the 90-s video segments, suspended particles do not have a simple back-and-forth oscillatory movement. Rather, the particles seem to make turns (of an acute angle) before (as well as after) accelerating and decelerating. Replacing the two wave trains with spectral waves, the properties of the linear summation should still

hold true except that the near-bed movement of water particles is more complicated than what is plotted in Fig. 12. It is hard to imagine that such bottom orbital movement can produce two sets of distinct ripples.

### 5.3. Hydrodynamic controls on sand ripples

The overall controls of directional wave spectra on sand ripples are far more complicated than the simplified depictions of Figs. 11 and 12. As both the processes and the products of sediment transport, properties of sand ripples are inevitably controlled by sediment transport. The ripple orientation appears to be in the direction of the maximum total sediment transport (Rubin and Ikeda, 1990; Gallagher et al., 1998). During the high sediment transport events of the two storms (Fig. 10, January 22–23, 30–31), the ripple orientations were in alignment with the wave directions. The directional spectra of these storm waves had a narrow frequency band of swells and a wide frequency band of seas whose energy overwhelmed the swells, but the directional spreading of these spectra were as narrow as  $20^\circ$ . Thus, the total sediment transport was in the direction of the storm waves. During swell-dominant wave conditions, the ripple orientations were in a large angle with the peak wave direction and with the azimuth of the near-bed orbital velocity. Mean currents, which are ignored due to its low (5–10 cm/s) magnitude, might have contributed to change the sediment transport direction, but given the fact that these swell-dominant waves had a capability of sediment transport several times to an order of magnitude smaller than the storm waves, one plausible explanation for the discrepancy of directions is that the hydrodynamics and the sand ripples were not in equilibrium. The less energetic swells with low sediment transport rate slowly reshaped and realigned the sand ripples created by previous high sediment transport events, but because of their low sediment transport rate, the swell-dominant waves were only able to change the shape but unable to change the orientation of the ripples to align with the swells. In other words, the ripple orientation observed during low energetic

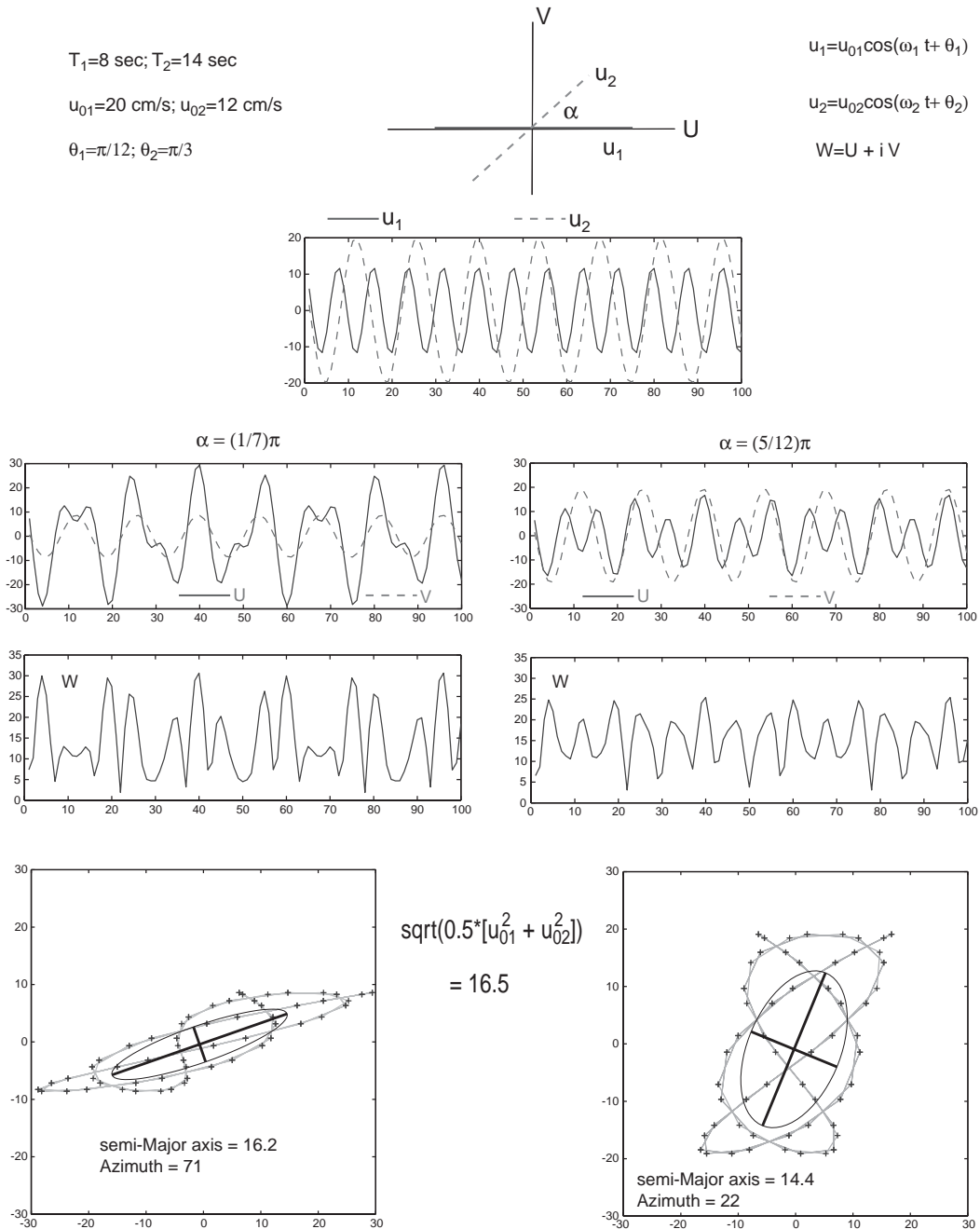


Fig. 12. A simplified scenario demonstrating the effect of the angle,  $\alpha$ , between two wave trains of different frequency on the combined bottom orbital velocity and therefore the orbital diameter. The top part of the figure shows the two wave trains and their characteristics. The bottom part of the figure is divided into two sections, each for one arbitrary  $\alpha$  value. Plotted in each section are: the two orthogonal velocity components  $U$  and  $V$ , the amplitude of speed  $W$ , the water particle traces and the velocity ellipses. Increasing the angle  $\alpha$  between two wave trains reduces the bottom orbital velocity.

wave conditions might be more related to the immediately prior high energetic waves.

Despite the attempt to correlate ripple types with wave types (Table 2), the controlling mechanisms of wave spectra on sand ripples are not fully understood. It is apparent from the observations presented here that vortex ripples (types 1 and 3) are created by high sediment transport events, and 2-D vortex ripples (type 1) appears to be related to higher sediment transport than 3-D vortex ripples (types 2 and 3). As for the response of ripples to the changes of spectral properties of the waves, it probably can only be determined in controlled laboratory experiments.

## 6. Conclusions

The following conclusions may be drawn based on the analyses presented in previous sections:

- The majority of observed sand ripples are sharp-crested, 2-D or 3-D vortex ripples. They primarily occurred under poly-modal wave environments (wave types B and C). In contrast, non-vortex (round and smooth crest) ripples were found mainly in swell-dominated conditions, especially wave type A. Brick-pattern ripples were found in a few video frames when type B waves prevailed, but this special pattern did not occur at other times with similar wave conditions.
- The sand ripples at this site on the San Pedro shelf are all anorbital. This is primarily due to the small grain sizes that result in a  $d_0/D_{50}$  ratio always greater than 5000. The ripple spacings are small (4.5–7.5 cm) and can be well represented by an empirical formula  $\lambda = 600D_{50}$ , which is a slight modification from Wiberg and Harris (1994) formula for anorbital ripples.
- Ripple orientations varied in a much smaller range ( $20^\circ$ ) than waves ( $90^\circ$ ), and this variation is better correlated with azimuth of the orbital velocities than the peak wave directions. Ripple orientation appears to be in the direction of the maximum sediment transport during high sediment transport events. Ripple orientation observed during low energetic wave conditions do not seem to be in equilibrium with the wave conditions and may be more related to the immediately prior high energetic waves.

- Use of the peak parameters (frequency, direction) from surface wave measurements to represent poly-modal, multi-directional spectral waves could lead to significant errors in computing sediment transport within bottom boundary layers. During the 20-day period, the peak wave periods measured from the surface elevation spectra are four or more seconds shorter than the peak periods measured from the bottom orbital velocity spectra (an underestimation of 25%) in at least 10% of data. Using spectral methods (e.g., Massel, 1996) can avoid this type of inaccuracies.

## Acknowledgements

The data come from the Huntington Beach Investigation project that is co-funded by the USGS and Orange County Sanitation District. Marlene Noble, Marinna Martini, Joanne Ferreira, Dave Gonzales and Jonathon Borden designed and implemented the experiments. Dan Hanes and Jodi Harney reviewed the manuscript. Comments from the journal reviewers and discussions with Dave Rubin have significantly improved the manuscript. Detong Sun is acknowledged for motivations on scratching the poly-modal, multi-directional spectral mess. Brandon Strong of RDI helped to unlock some of the secrets in his WaveMon and WaveView software. Field assistances from the skillful crew on R./V. *Robert Gordon Sproul* are very much appreciated.

## References

- Allen, J.R.L., 1982. *Sedimentary Structures: Their Character and Physical Basis*, I. Elsevier, Amsterdam (593pp).
- Amos, C.L., Bowen, A.J., Huntley, D.A., Lewis, C.F.M., 1988. Ripple generation under the combined influences of waves and currents on Canadian continental shelf. *Continental Shelf Research* 8 (10), 1129–1153.
- Boyd, R., Forbes, D.L., Heffler, D.E., 1988. Time-sequence observations of wave-formed sand ripples on an ocean shoreface. *Sedimentology* 35, 449–464.

- Cacchione, D.A., Southard, J.B., 1974. Incipient sediment movement by shoaling internal gravity waves. *Journal of Geophysical Research* 70, 2237–2242.
- Carstens, M.R., Neilson, F.M., Altinbilek, H.D., 1969. Bedforms generated in the laboratory under an oscillatory flow: analytical and experimental study. Technical Memo 28, US Army Corps of Engineering, Coastal Engineering Research Center, Washington, DC (39pp).
- Clifton, H.E., 1976. Wave-formed sedimentary structures: a conceptual model. In: Davis Jr., R.A., Ethington, R.L. (Eds.), *Beach and Nearshore Sedimentation*, vol. 24. SEPM Special Publication, pp. 126–148.
- Clifton, H.E., Dingler, J.R., 1984. Wave-formed structures and paleoenvironmental reconstruction. *Marine Geology* 60, 165–198.
- Dingler, J.R., 1974. Wave-formed ripples in nearshore sands. Ph.D. Thesis, University of California, San Diego (136pp).
- Drake, D.E., Cacchione, D.A., Karl, H.A., 1985. Bottom currents and sediment transport on San Pedro shelf, California. *Journal of Sedimentary Petrology* 55, 15–28.
- Faraci, C., Foti, E., 2002. Geometry, migration and evolution of small-scale bedforms generated by regular and irregular waves. *Coastal Engineering* 47, 35–52.
- Grant, W.D., Madsen, O.S., 1982. Movable bed roughness in unsteady oscillatory flow. *Journal of Geophysical Research* 87 (C1), 469–481.
- Gallagher, E.L., Elgar, S., Thornton, E.B., 1998. Megaripple migration in a natural surf zone. *Nature* 394, 165–168.
- Hamilton, P., Singer, J.J., Waddell, E., Robertson, G., 2001. Circulation processes on the San Pedro shelf. *Proceedings of the Oceans 2001 MTS/IEEE Conference*, 2001–2008.
- Hay, A.E., Wilson, D.J., 1994. Rotary sidescan images of nearshore bedform evolution during a storm. *Marine Geology* 119, 57–65.
- Horrer, P.L., 1950. Southern Hemisphere swells and waves from a tropical storm at Long Beach, California. *US Army Corps of Engineering, Beach Erosion Board Bulletin* 4 (3), 1–18.
- Inman, D.L., 1957. Wave generated ripples in nearshore sands. Technical Memo 100, US Army Corps of Engineering, Beach Erosion Board, Washington, DC (66pp).
- Inman, D.L., Bowen, A.J., 1963. Flume experiments on sand transport by waves and currents. *Coastal Engineering, Proceedings of the Eighth Conference*. American Society of Civil Engineering, New York, pp. 1123–1142.
- Jette, C.D., Hanes, D.M., 1996. Measurements of wave generated bedforms. *Coastal Engineering, Proceedings of the 25th Conference*. American Society of Civil Engineering, New York, pp. 3129–3142.
- Karl, H.A., 1976. Processes influencing transportation and deposition of sediment on the continental shelf, southern California. Ph.D. Thesis, University of Southern California, Los Angeles (331pp).
- Karl, H.A., Cacchione, D.A., Drake, D.E., 1980. Erosion and transport of sediments and pollutants in the benthic boundary layer on the San Pedro shelf, southern California. Open-File Report 80–386, US Geological Survey (54pp).
- Lofquist, K.E.B., 1978. Sand ripple growth in an oscillatory-flow water tunnel. Technical Paper 78-5, US Army Corps of Engineering, Coastal Engineering Research Center, Washington, DC.
- Massel, S.R., 1996. *Ocean Surface Wave: Their Physics and Prediction*. World Scientific, Singapore (491pp).
- Miller, M.C., Komar, P.D., 1980. A field investigation of the relationship between oscillation ripple spacing and the near-bottom water orbital motions. *Journal of Sedimentary Petrology* 50, 183–191.
- Mogridge, G.R., Kamphuis, J.W., 1972. Experiments on bedform generation by wave action. *Coastal Engineering, Proceedings of the 13th Conference*. American Society of Civil Engineering, New York, pp. 137–150.
- Nielsen, P., 1981. Dynamics and geometry of wave-generated ripples. *Journal of Geophysical Research* 86 (C7), 6467–6472.
- Nielsen, P., 1992. *Coastal Bottom Boundary Layers and Sediment Transport*. World Scientific, Singapore (324pp).
- Noble, M.A., Xu, J.P., Rosenfeld, L.K., Largier, J., Hamilton, P., Jones, B.L., Robertson, G.L., 2003. Huntington beach shoreline contamination investigation, Phase III, Executive Summary. Open-File Report 03-62, US Geological Survey (20pp).
- Osborne, P.D., Vincent, C.E., 1993. Dynamics of large and small scale bedforms on a macrotidal shoreface under shoaling and breaking waves. *Marine Geology* 115, 207–226.
- RD Instruments, 2001. *Waves User's Guide*. P/N 957-6148-00 (April 2001), RD Instruments, San Diego, CA (74pp).
- Rorbaek, K., Andersen, H., 2000. Evaluation of wave measurements with an acoustic Doppler current profiler. *Proceedings of the Oceans 2000 MST/IEEE Conference*, pp. 1181–1187.
- Rubin, D.M., Ikeda, H., 1990. Flume experiments on the alignment of transverse, oblique, and longitudinal dunes in directionally varying flows. *Sedimentology* 37, 673–684.
- Sleath, J.F.A., 1984. *Sea Bed Mechanics*. Wiley, New York.
- Soulsby, R.L., 1987. Calculating bottom orbital velocity beneath waves. *Coastal Engineering* 11, 371–380.
- Soulsby, R.L., 1997. *Dynamics of Marine Sands*. Thomas Telford, London (249pp).
- Strong, B., Brumley, B.H., Terray, E.A., Stone, G.W., 2000. The performance of ADCP-derived wave spectra and comparison with other independent measurements. *Proceedings of the Oceans 2000 MST/IEEE Conference*, pp. 1195–1203.
- Traykovski, P., Hay, A.E., Irish, J.D., Lynch, J.F., 1999. Geometry, migration, and evolution of wave orbital ripples at LEO-15. *Journal of Geophysical Research* 104 (C1), 1505–1524.
- Terray, E.A., Brumley, B.H., Strong, B., 1999. Measuring waves and currents with an upward-looking ADCP. *Proceedings of the IEEE Sixth Working Conference*

- on Current Measurement. IEEE Press, New York, pp. 66–71.
- Wiberg, P.L., Harris, C.K., 1994. Ripple geometry in wave-dominated environments. *Journal of Geophysical Research* 99 (C1), 775–789.
- Willis, D.H., Davies, M.H., Mogridge, G.R., 1993. Laboratory observations of bedforms under directional irregular waves. *Canadian Journal of Civil Engineering* 20, 550–563.
- Yalin, M.S., Russell, R.C., 1962. *Mechanics of Sediment Transport*, second ed. Pergamon, New York (247pp).